PAPER

Bacteria-inspired magnetically actuated rod-like soft robot in viscous fluids

To cite this article: Anuruddha Bhattacharjee *et al* 2022 *Bioinspir. Biomim.* **17** 065001

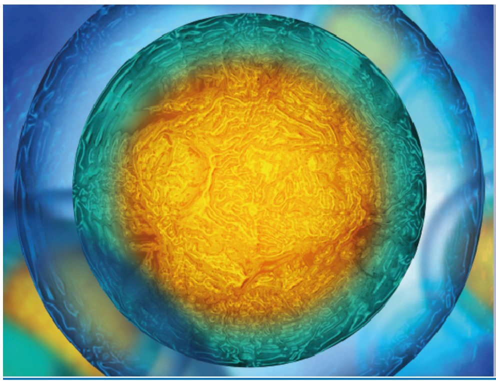

IOP Publishing Bioinspir. Biomim. 17 (2022) 065001 https://doi.org/10.1088/1748-3190/ac870f

Bioinspiration & Biomimetics

CrossMark

RECEIVED
13 March 2022

REVISED
15 June 2022

ACCEPTED FOR PUBLICATION
4 August 2022

PUBLISHED
12 September 2022

PAPER

Bacteria-inspired magnetically actuated rod-like soft robot in viscous fluids

Anuruddha Bhattacharjee[1], Mehdi Jabbarzadeh[2], Gokhan Kararsiz[1], Henry C Fu[2] and Min Jun Kim[1,*]

[1] Department of Mechanical Engineering, Southern Methodist University, Dallas, TX 75205, United States of America
[2] Department of Mechanical Engineering, The University of Utah, Salt Lake City, UT 84112, United States of America
[*] Author to whom any correspondence should be addressed.

E-mail: mjkim@lyle.smu.edu

Keywords: magnetic swimmer, hydrogel soft robots, low *Re* propulsion

Supplementary material for this article is available online

Abstract

This paper seeks to design, develop, and explore the locomotive dynamics and morphological adaptability of a bacteria-inspired rod-like soft robot propelled in highly viscous Newtonian fluids. The soft robots were fabricated as tapered, hollow rod-like soft scaffolds by applying a robust and economic molding technique to a polyacrylamide-based hydrogel polymer. Cylindrical micro-magnets were embedded in both ends of the soft scaffolds, which allowed bending (deformation) and actuation under a uniform rotating magnetic field. We demonstrated that the tapered rod-like soft robot in viscous Newtonian fluids could perform two types of propulsion; boundary rolling was displayed when the soft robot was located near a boundary, and swimming was displayed far away from the boundary. In addition, we performed numerical simulations to understand the swimming propulsion along the rotating axis and the way in which this propulsion is affected by the soft robot's design, rotation frequency, and fluid viscosity. Our results suggest that a simple geometrical asymmetry enables the rod-like soft robot to perform propulsion in the low Reynolds number ($Re \ll 1$) regime; these promising results provide essential insights into the improvements that must be made to integrate the soft robots into minimally invasive *in vivo* applications.

1. Introduction

The incorporation of soft and flexible materials into conventional robotics has garnered much excitement over the years, promising to overcome many challenges inherent to conventional rigid robots [1–6]. Flexible structures allow soft robots to be morphologically adaptable in complex environments and swim at a low Reynolds number (*Re*), where viscous force dominates over inertia [7]. Moreover, miniature soft robots that can perform bioinspired locomotion modes, such as swimming [4, 8–10], rolling [1, 11], crawling [2, 12–14], jumping [15, 16], and climbing [17], have great potential for targeted drug release [18], endoscopy [19, 20], and minimally invasive surgery [21, 22]. In recent years, a lot of exciting research has been conducted to develop wireless miniature soft robots powered by external stimuli, which include magnetic [2, 4, 8, 10, 12, 13, 17, 23, 24], acoustic [25, 26], light [16, 18, 27], thermal [15], and chemical [28]. Among these, magnetic stimuli-based control systems are prominent and well suited for biomedical applications, as the actuating magnetic fields can easily and harmlessly penetrate most biological materials [29, 30]. Although recent advances have shown great promise and developed state-of-the-art soft robotics at mesoscale (milli-/microscale), only a few demonstrated locomotion in the unique hydrodynamic environment of highly viscous Newtonian fluids ($Re \ll 1$). Therefore, we seek to explore the locomotive dynamics of a newly developed magnetically actuated rod-like soft robot (a tapered hydrogel soft body with embedded permanent micro-magnets) at low *Re* propulsion conditions. Table 1 summarizes recently reported soft magnetic swimmers at mesoscale, along with the contributions of our current work.

Table 1. A summary of recently reported magnetically actuated soft swimmers at mesoscale.

Type/shape	Robot size	Material	Test fluid	Contributions
Tubular body and helical tail [8]	Length < 3 mm	Poly (ethylene glycol) diacrylate and N-isopropyl acrylamide hydrogel layer with magnetic nanoparticles	Sucrose solution (viscosities of 3 mPa s and 15 mPa s)	Robot design and locomotion at low *Re* (10^{-2} to 10^{-4})
Sheet-shaped [9]	Length 2 to 4.5 mm, thickness 0.03 to 0.1 mm	Ecoflex 00-50 and permanent magnetic microparticles	Water	Deformation modeling of a magnetic sheet for under-water swimming
Jellyfish-like [4]	Diameter 3 mm	Ecoflex 00-10 and NdFeB magnetic microparticles	Water	Lappet kinetics and object manipulation
Sheet-shaped [24]	Length 3.5 to 10.5 mm, width 1 mm, thickness 0.24 mm	Ecoflex 00-10 and NdFeB magnetic microparticles	Viscous fluid (glycerol with viscosity, $\mu = 6$ cSt, 343 cSt, and 720 cSt) and shear-thinning fluid (hyaluronic acid sodium solution)	Motion dynamics in fluid-filled confined spaces
Shuttle-shaped (Zebrafish-like)[10]	Length of major axis: 15 mm	Ecoflex 00-30 and NdFeB composites	Water	Robot design, fish-like swimming, and camouflage ability
Tapered, hollow rod-like (this work)	Length 10 mm, diameter 1 to 1.2 mm	Polyacrylamide hydrogel and neodymium (Nd) permanent micro-magnets	Viscous fluids (glycerin with $\mu = 1000$ cSt and silicone oil with $\mu = 10\,000$ cSt)	Robot design and swimming kinetics at low *Re* (0.0002 to 0.07)

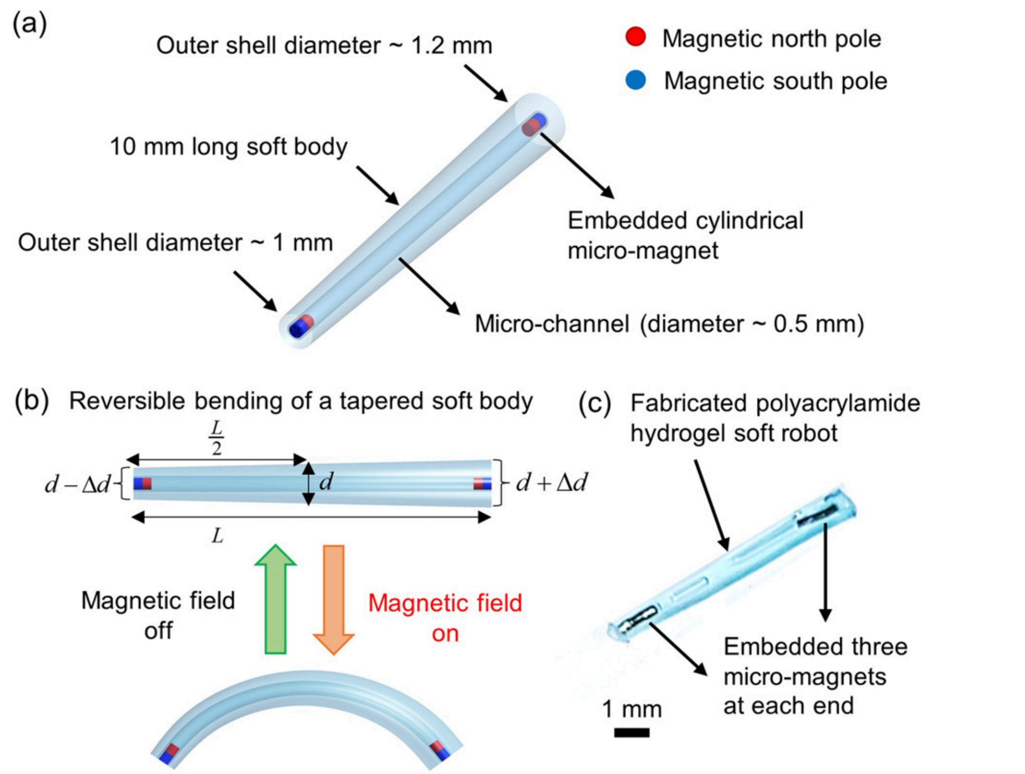

Figure 1. Design and fabrication of a tapered rod-like soft robot. (a) A schematic showing design concept of a rod-like soft robot with a tapered soft body and embedded micro-magnets at both ends. (b) A tapered soft body with embedded magnets of alternating polarity at ends can change its shape (by reversible bending) under an external magnetic field. (c) A fabricated soft robot (10 mm long) made of polyacrylamide hydrogel and embedded with three micro-magnets at each end.

It is necessary to comprehend the fluid dynamics of small-scale locomotion to understand the biophysics of swimming microorganisms. For example, the motility of bacteria, such as *Escherichia coli* [31], *Borrelia burgdorferi* [32], and *Vibrio* species [33], affects their ability to colonize and infect our bodies. Microorganisms are small and slow enough that their fluid dynamics occur in the low Reynolds number regime ($Re = 10^{-6}$ for *E. coli*, and $Re = 10^{-4}$ for sperm) [7, 34]. In such a low Reynolds number (viscosity-dominated regime), Purcell [7] showed that for microorganisms to swim, they must perform non-reciprocal strokes that do not follow the same sequence of configurations going forward and backward in time. Microscale robotic systems (microbots) inspired by swimming microorganisms have been designed to use flexibility to induce non-reciprocal motions [23, 35, 36], even from reciprocal actuating forces such as a planar oscillating magnetic field. However, actuation by a rotating external magnetic field is inherently non-reciprocal since rotation reverses direction under time reversal. For such non-reciprocal rotary actuation, it has been discovered that certain geometric requirements prevent straight rod-like microbots from achieving propulsion along the rotation axis [37]. In that case, adding flexibility to a straight rod can allow the microbot to deform into geometries that are capable of such propulsion.

Taking design inspiration from bacteria such as *Bacillus* [37, 38] and *Spirochetes* [39, 40], we formed a polyacrylamide-based hydrogel polymer into a flexible, tapered rod-like structure and embedded micro-magnets at each end to allow the structure to be actuated by a rotating magnetic field. We demonstrate two types of propulsion in highly viscous Newtonian fluids (with viscosities 1000 cSt (centistokes) and 10 000 cSt): rolling near a boundary and swimming far away from any boundary. We apply numerical simulations of the swimming motion along the rotation axis to understand the design requirements for such rod-like soft robots to be capable of swimming and how their swimming propulsion (along the rotation axis) is affected by the taper dimension, rotational frequency, and fluid viscosity. Our results provide interesting insights into how such soft robots may be improved in the future for potential applications.

2. Methods

2.1. Design and fabrication process

Informative aspects of the rod-like soft robot with embedded micro-magnets at both ends can be viewed in figure 1, which displays its design concept [figure 1(a)], its shape-changing capability that includes a reversible bending by an external magnetic field [figure 1(b)], and a fabricated version of the soft robot made of polyacrylamide hydrogel [figure 1(c)].

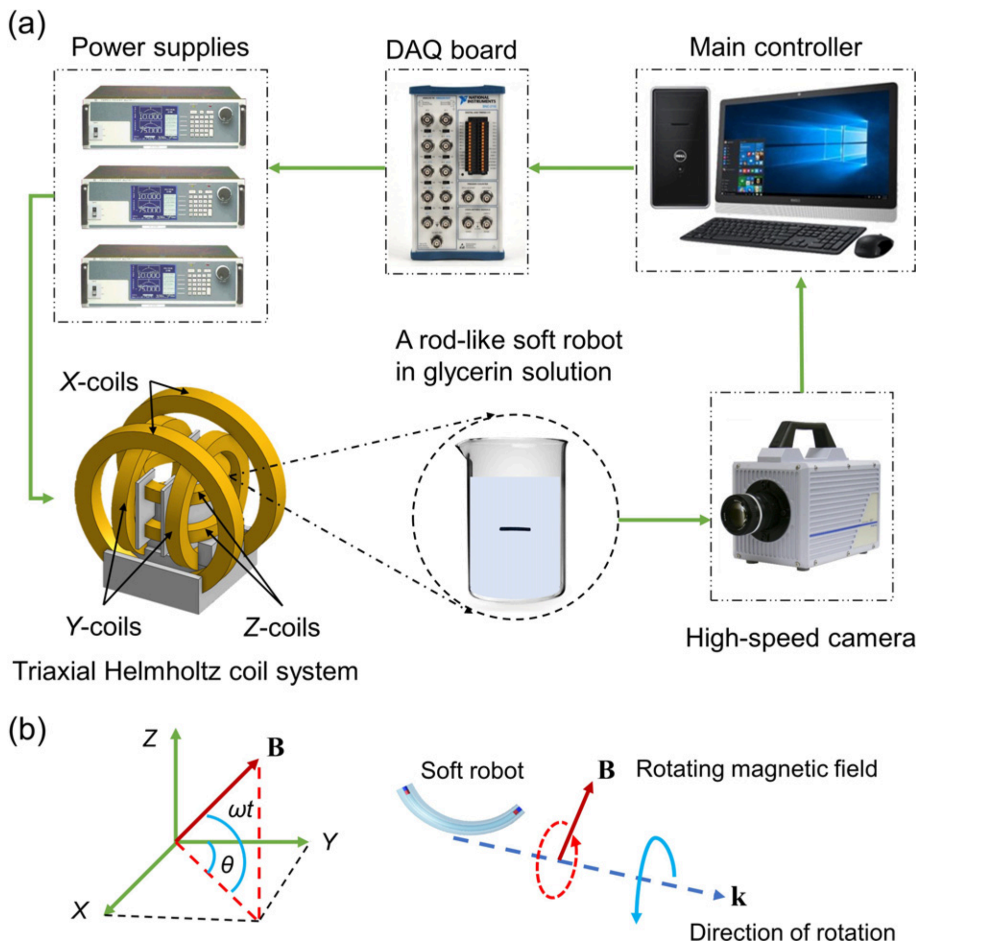

Figure 2. (a) A schematic of the experimental setup, including the main controller, DAQ board, three power supplies, the Helmholtz coil system along with a soft robot in a glass beaker at the core, and a high-speed camera. (b) A schematic showing applied rotating magnetic field in the XYZ coordinate system.

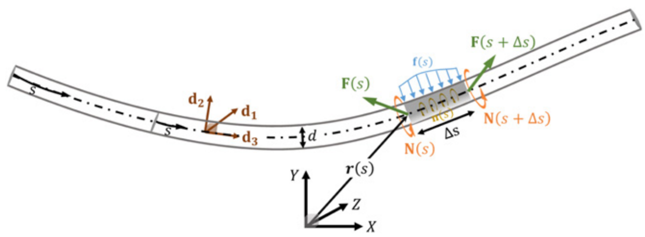

Figure 3. A schematic of the rod-like soft robot described as an inextensible Kirchhoff rod.

The proposed design has a hollow and tapered rod-like soft body with varying diameters along its length. Cylindrical micro-magnets embedded into both ends of the soft body allow for an alternating magnetic polarity that enables an external magnetic field to reversibly control the bending of the body by turning the field on and off, as shown in figure 1(b).

The rod-like soft scaffolds were fabricated using polyacrylamide-based hydrogel following a robust and economic molding technique. First, the hydrogel polymer was prepared by combining a gel mixture with a precursor mixture. The gel mixture consisted of 23 μL of bis-acrylamide (OmniPur® Acrylamide: Bis solution 29:1 40% solution, calbiochem), 12 μL of 1.5% APS (ammonium persulfate), and 2 μL of SDS (sodium dodecyl sulfate). The precursor mixture consisted of 0.2 μL of TEMED (tetramethyl ethylenediamine) and 32 μL of 1 M HEPES solution. A borosilicate glass Pasteur pipet (Fisherbrand^{TM}, 14.6 cm long) was used to draw the combined gel and precursor mixture through capillary action. The mixture was then cured into a flexible polymeric structure inside the pipet, which functioned as its mold. The shape of the glass pipet dictated variation in the diameter of the rod-like soft scaffold. Therefore, before drawing the polymeric mixture into the glass

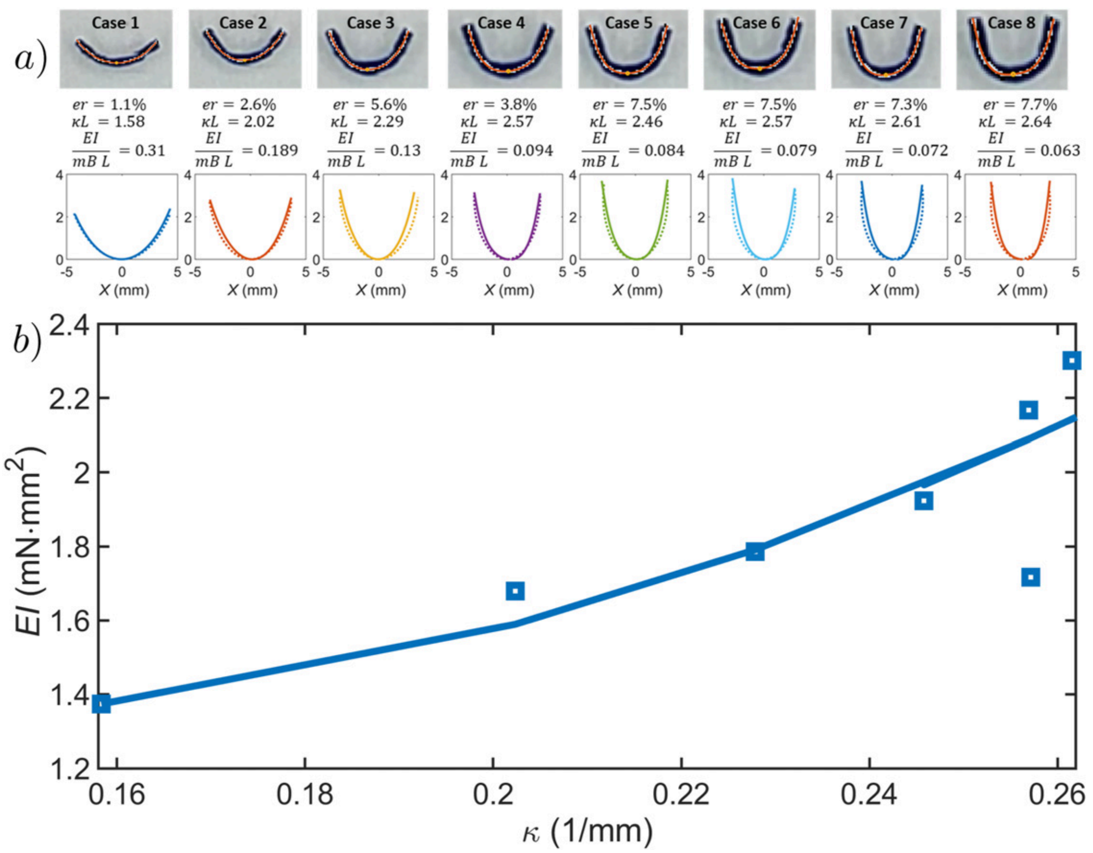

Figure 4. Estimation for optimal bending stiffness from the static experiments. (a) Top panel: steady state deformed shapes of the soft robot under different external magnetic fluxes, $B = (3.6, 7.3, 11.2, 15.0, 18.7, 22.4, 26.1, 29.6)$ mT for corresponding cases 1 to 8. The orange line represents the centerline of the robot used for comparison with simulations. Bottom panel: simulated shapes for the centerline of the soft robot using Kirchhoff rod model under external magnetic field, with associated errors (er) obtained by using (16) corresponding to different cases in the top panel. (b) Bending stiffness as a function of curvature. The square symbols represent estimated bending stiffness and curvature for different cases in (a), and the solid line describes second order polynomial fit for the calculated data.

pipet, a thin and straight copper wire (with a diameter of 0.45 mm) was placed at the center of the pipet (using 3D-printed fixtures); its later removal formed the micro-channel at the core of the soft scaffold. Once the hydrogel mixture was cured inside the glass pipet for 10 min, compressed air from a fume hood outlet was used to blow the rod-like soft scaffold out of the glass pipet. Then the copper wire was removed, and the hydrogel scaffold was preserved in deionized water for swelling. After 30 min of swelling in water, the rod-like scaffold was taken out of the water and was cut to a 10 mm long flexible rod with a diameter (d) varying from 1 to 1.2 mm along its length. At both ends, three cylindrical nickel-coated permanent micro-magnets were embedded into the micro-channel, each having a diameter of 0.3 mm, a height of 0.5 mm, and the strength of neodymium 52. A fabricated hydrogel soft body is typically transparent; therefore, blue food dye was added to its water bath before/during the swelling phase to increase visibility and enable tracking. A fabricated hydrogel soft robot with embedded cylindrical micro-magnets at both ends is shown in figure 1(c).

2.2. Magnetic control system and experimental procedures

A large-scale nested, triaxial Helmholtz coil system was utilized to generate the magnetic fields while conducting experiments. Figure 2(a) shows a schematic of the experimental setup, including the main controller, National Instruments data acquisition (DAQ) board, three power supplies, the Helmholtz coil system along with a soft robot in a glass beaker (VWR®, capacity: 400 mL, height: 106 mm, outer diameter: 77 mm) at the core, and a high-speed camera. The triaxial Helmholtz coil system was designed following the specifications that are listed in [38]. The coil system has three pairs of coils labeled as X-coils, Y-coils, and Z-coils based on the centerlines of the coil pairs. Each coil pair is connected to a power supply (Kepco, BOP 50-20 MG). A customized C++ program was used to control signal outputs to the interfaced DAQ board, which directs the signals to the attached power supplies to create a uniform rotating magnetic field at the core of the coils with time-dependent magnitude and frequency. A uniform rotating magnetic field generated

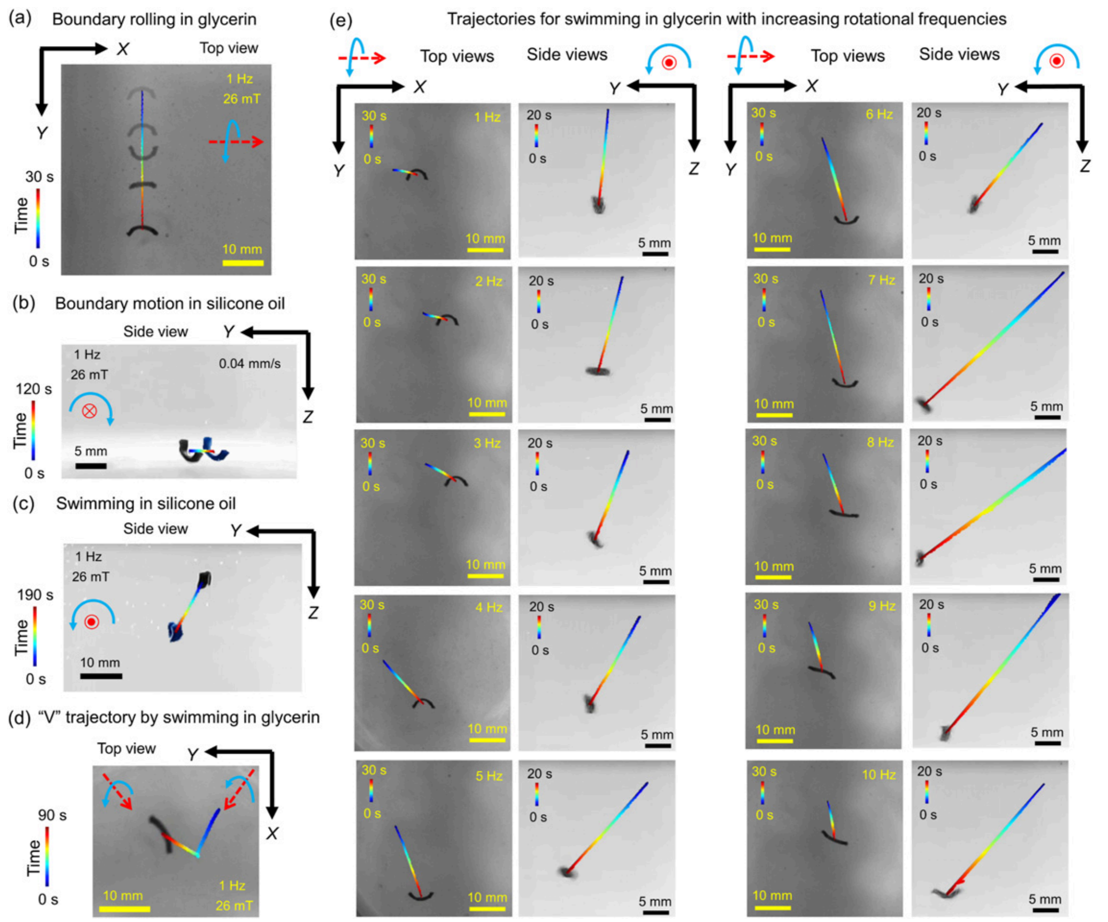

Figure 5. Motion trajectories of a rod-like soft robot for boundary motion/rolling and swimming in viscous fluids. (a) A top view showing boundary rolling of the soft robot in glycerin for a rotating magnetic field of 26 mT at 1 Hz about the positive X-axis. (b) A boundary motion of the soft robot (different than rolling) is observed in silicone oil. In this case, a rotating magnetic field of 26 mT at 1 Hz about the negative X-axis creates propulsion along the negative Y-axis. (c) A side view showing trajectory while swimming in silicone oil under a magnetic rotation about the positive X-axis. (d) A soft robot swimming in 'V' trajectory under open-loop control. (e) Top and side views showing swimming trajectories in glycerin with increasing rotational frequencies (i.e., from 1 to 10 Hz) under a uniform rotating magnetic field at 26 mT about the positive X-axis. The axis and sense of rotation of the applied magnetic field are depicted in figures by either red arrow or dot/cross and blue arrow, respectively. Reynolds number (Re) for the experiments was calculated by using (3) and was found to be in the range of 0.0002 to 0.07, ensuring a low Re propulsion condition. See the attachment for videos of these demonstrations.

by the Helmholtz coil system can be described by

$$\mathbf{B} = \begin{bmatrix} B_X \\ B_Y \\ B_Z \end{bmatrix} = \begin{bmatrix} B\,\sin(\theta)\cos(\omega t) \\ B\,\cos(\theta)\cos(\omega t) \\ B\,\sin(\omega t) \end{bmatrix}, \quad (1)$$

$$\mathbf{k} = \begin{bmatrix} -\cos(\theta) & \sin(\theta) & 0 \end{bmatrix}, \quad (2)$$

where $\mathbf{B}$ is the magnetic field vector, B_X, B_Y, and B_Z are the three-dimensional components along the X-, Y-, and Z-axes, respectively, B is the amplitude of the rotating magnetic field, ω is the frequency (rad s^{-1}), t is the time (s), θ is the angle (rad) between the Y-axis and the plane of rotation, and $\mathbf{k}$ is the vector along the rotation axis [figure 2(b)].

The first set of experiments involved static bending tests under incrementally increasing magnetic fluxes, applying static magnetic fields to an initially straight rod-like soft robot submerged in deionized water. Data from these experiments were used to optimize the numerical model's bending stiffness (EI).

Next, several experiments were performed to observe and analyze the propulsion characteristics of a 10 mm long, rod-like soft robot in highly viscous fluids, such as glycerin and silicone oil that maintain the propulsion conditions at a low Reynolds number ($Re = \frac{\text{Intertial forces}}{\text{Viscous forces}} \ll 1$). Re for different experiments can be calculated by

$$Re = \frac{\rho r_{\max}\omega L}{\mu}, \quad (3)$$

where ρ is the density of the experimental fluid, $r_{\max}$ is the maximum deflection from the axis of rotation, ω is the rational frequency (rad s^{-1}), L is the length of the soft robot, and μ is the fluid viscosity. For different experiments, the calculated Re was in the range of 0.0002 to 0.07. A rotating magnetic field was applied with increasing field frequency to create motion for propulsion experiments. The magnitude of the rotating magnetic field was kept constant at 26 mT, while the frequency (ω) was incremented from

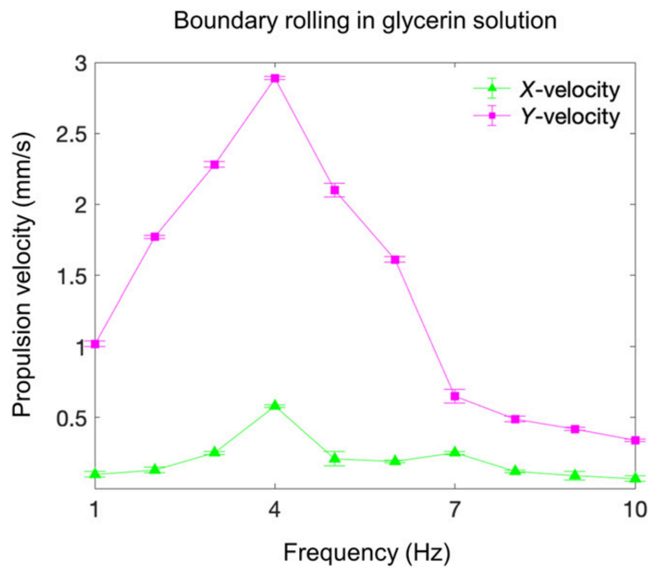

Figure 6. Propulsion velocity along vs rotating magnetic field frequency for boundary rolling in glycerin solution. At least five trials were performed for each rotating frequency. Data are presented as mean ± standard deviation.

+1 Hz to +10 Hz at 1 Hz increments $(\omega = 2\pi f$, where f is the frequency in Hz). A high-speed camera (Photron, FASTCAM SA3 Model 60 K) was used to capture videos from the top at 125 fps (frames per second), while another digital camera (Logitech, C922 Pro) was used to capture videos from the sides at 30 fps. In the videos, the centroid of a soft robot (in motion) was tracked through binary image processing using MATLAB, and propulsion velocities were calculated by dividing the displacement of the centroid between frames by the sampling time (1/125 s and 1/30 s for videos from the top and front cameras, respectively).

2.3. Numerical inextensible model

Since the fluid flows occur in the low Reynolds number regime, we model them using the Stokes equations,

$$0 = -\nabla p + \nabla^2 \mathbf{v}. \tag{4}$$

All equations in this section 2.3 are written in nondimensional form, with lengths measured in units of the rod length L, velocity field ($\mathbf{v}$) measured in units of ωL, and fluid pressures and stresses measured in units of $\mu\omega$, where μ is the fluid viscosity. We solve the hydrodynamics using the method of regularized Stokeslets [39, 40]. In this method, we discretize the rod into cylindrical segments of length Δs, and then discretize the outer surface of each segment with 64 regularized Stokeslets. Each regularized Stokeslet exerts a force on the fluid, and the total flow is the superposition of the flows arising from all the regularized Stokeslets. This method was previously used to simulate the biolocomotion of the bacteria *B. subtilis* [41], *V. alginolyticus* [42], *H. pylori* [43], and *H. suis* [44], as well as microrobots [37, 45]. Details about our implementation of the method of regularized Stokeslets can be found in the literature [41, 46, 47].

We model the bending of the rod-like soft robot as an inextensible Kirchhoff rod [figure 3], which has a centerline described by the position $\mathbf{r}(s)$, where s is the arclength (measured in units of rod length L) along the rod centerline, and an orthonormal triad at each cross-section that rotates with the material of the rod, $\mathbf{d}^1, \mathbf{d}^2, \mathbf{d}^3$. The third member of the triad, $\mathbf{d}^3 = \partial_s \mathbf{r}(s)$, is the unit vector tangent to the centerline. The Kirchhoff rod equations express force and torque balance on the rod

$$0 = \partial_s \mathbf{F}(s) + \mathbf{f}(s), \tag{5}$$

$$0 = \partial_s \mathbf{N}(s) + \mathbf{d}^3 \times \mathbf{F}(s) + \mathbf{n}(s), \tag{6}$$

where $\mathbf{F}(s)$ is the elastic force (measured in units of $\mu\omega L^2$) exerted by material with larger s on material and smaller s at the cross-section at a position s, $\mathbf{f}(s)$ is the external force per unit length (measured in units of $\mu\omega L$) exerted on the rod by the fluid, $\mathbf{N}(s)$ is the torque (measured in units of $\mu\omega L^3$) exerted by material with larger s on material and smaller s at the cross-section at a position s, and $\mathbf{n}(s)$ is the external torque per unit length (measured in units of $\mu\omega L^2$) exerted on the rod by the fluid. The cross-sectional torques are determined by the constitutive laws as follows,

$$Sp^4 N_1 = \partial_s \mathbf{d}^2 \cdot \mathbf{d}^3, \tag{7}$$

$$Sp^4 N_2 = \partial_s \mathbf{d}^3 \cdot \mathbf{d}^1, \tag{8}$$

$$Sp^4 N_3 = \gamma \partial_s \mathbf{d}^1 \cdot \mathbf{d}^2. \tag{9}$$

The parameter γ is the ratio of torsional stiffness (GJ) to bending stiffness (EI) of the rod, where G is the shear modulus, E is Young's modulus, and J and I are the second moments of area of the rod's

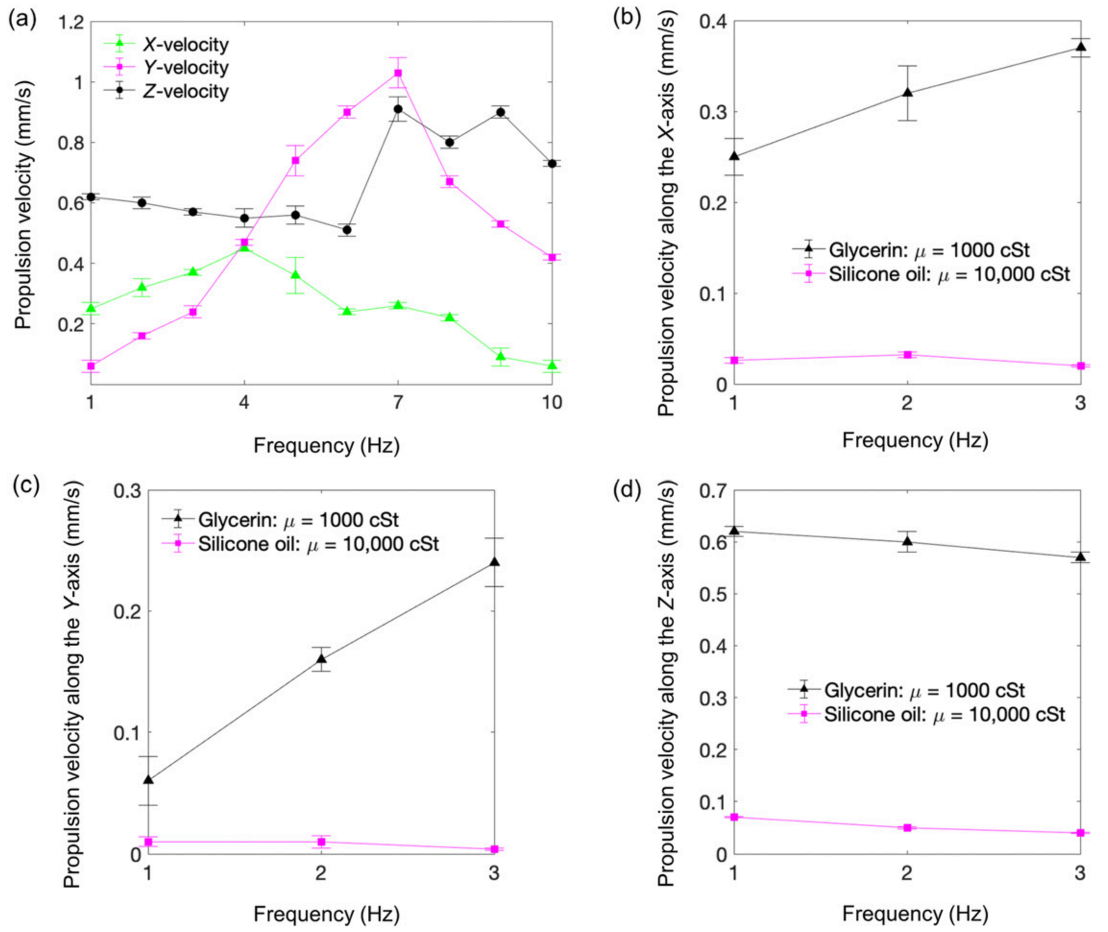

Figure 7. Effect of rotating frequency and fluid viscosity on swimming velocity. (a) Propulsion velocity vs rotating magnetic field frequency for swimming in glycerin solution. Propulsion velocity vs rotating magnetic field frequency for swimming by a soft robot (with 5% taper) in glycerin (viscosity $\mu = 1000$ cSt) and silicone oil (viscosity $\mu = 10\,000$ cSt) along the (b) X-axis, (c) Y-axis, and (d) Z-axis. At least five trials were performed for each rotating frequency. Data are presented as mean $\pm$ standard deviation.

cross-section with respect to the rod's centerline and diameter of the rod, respectively. Throughout the paper, we assume that $\gamma = 1$. The other parameter is the Sperm number,

$$Sp = \left(\frac{\mu L^4 \omega}{EI}\right)^{\frac{1}{4}}, \tag{10}$$

which varies in our experiments and simulations.

The no-slip boundary condition at the surface of the rod (specified by positions $\mathbf{r}_s$) requires that

$$\mathbf{v}(\mathbf{r}_s) = \mathbf{u}(\mathbf{r}_s), \tag{11}$$

where $\mathbf{u}(\mathbf{r}_s)$ is the dimensionless velocity of the rod surface. The hydrodynamic force and torque per unit length on a cylindrical segment are

$$\mathbf{f}(s) = \frac{1}{\Delta s}\int\int \boldsymbol{\tau}\cdot \mathrm{dA}, \tag{12}$$

$$\mathbf{n}(s) = \frac{1}{\Delta s}\int\int \mathbf{r}\times\boldsymbol{\tau}\cdot \mathrm{dA}, \tag{13}$$

where $\boldsymbol{\tau}$ is the fluid stress tensor, and the expressions are integrated over the surface of the cylinder. Together (11)–(13) couple the fluid and bending equations.

Finally, the rod-like soft robot is actuated by magnetic torques exerted on the first and last cross-sections at the very ends of the rod,

$$Ma\mathbf{N}_{\mathbf{end}} = (\hat{\mathbf{m}}\times\hat{\mathbf{B}}), \tag{14}$$

where $\hat{\mathbf{B}}$ is a unit vector in the direction of the magnetic field. The magnetic dipole at each end has a direction specified by $\hat{\mathbf{m}}$, which takes a fixed orientation relative to the tangent vector of the end segment. In (14), the parameter which appears is the Mason number,

$$Ma = \frac{\mu\omega L^3}{mB}, \tag{15}$$

that varies in our experiments and simulations. Here, B is the magnitude of the magnetic field, and the magnitude of the magnetic dipole at each end is $m = 122$ A mm^2.

These coupled equations were previously used to describe the deformation of bacterial flagella [44]. The results in this paper are obtained by solving the coupled set of equations numerically using the implementation described in detail in [47]. At each time step, this method determines each rod segment's translational and angular velocities from the current deformed configuration of the rod and the direction of the magnetic field, which we integrate forward in time to obtain the time-evolution dynamics of the soft robot. As a result, the soft robot's overall translational and angular velocities are obtained simultaneously and specified uniquely once a total force-free condition is applied.

2.4. Determination of bending stiffness

We used the observed bending of the rod-like soft robot under the application of a static magnetic field [5] to determine its bending stiffness. We used our numerical model with a constant non-rotating magnetic flux with an initially straight rod. We solved for the time evolution of the rod's shape until a steady state was reached. For each case (magnetic fluxes of 3.62 mT, 7.30 mT, 11.21 mT, 15.00 mT, 18.71 mT, 22.44 mT, 26.06 mT, and 29.64 mT), we tested different values of the bending stiffness and chose the optimal bending stiffness that minimized the error between the observed and simulated deformed shapes. Figure 4(a) shows the observed shapes overlaid with the simulated centerline of the optimal stiffness, as well as a comparison between the observed and simulated centerlines and the error between them,

$$\mathrm{er} = \sum_{i=1}^{n} \frac{\left|\mathbf{X}^i_{\mathrm{sim}} - \mathbf{X}^i_{\mathrm{exp}}\right|}{L}. \tag{16}$$

Finally, we calculated the curvature of the simulated shape and plotted the optimal stiffness as a function of curvature in figure 4(b). The bending stiffness increases from about 1.4 $\mathrm{mN \cdot mm^2}$ to 2.2 $\mathrm{mN \cdot mm^2}$ as the curvature increases from about 0.16 $\mathrm{mm^{-1}}$ to 0.26 $\mathrm{mm^{-1}}$, i.e., the rod-like hydrogel polymer displays strain stiffening behavior. However, for simplicity, we use a constant $EI = 2.11\ \mathrm{mN \cdot mm^2}$ for the remainder of the paper since this is the value of EI for case 7 at $B = 26.1$ mT, the value of magnetic field magnitude that all the swimming experiments used.

3. Results and discussion

3.1. A rod-like soft robot with a variation in diameter is asymmetric enough for propulsion

A rod-like soft robot, as shown in figure 1(c), was observed to translate while exposed to uniform rotating magnetic fields in highly viscous Newtonian fluids (i.e., 1000 to 10 000 times more viscous than water), such as 99% glycerin solution with a viscosity of $\mu_0 = 1000$ centistokes (cSt) and silicone oil with a viscosity of 10 000 cSt ($10\mu_0$). As shown in figure 5, when a rotating magnetic field at a specific

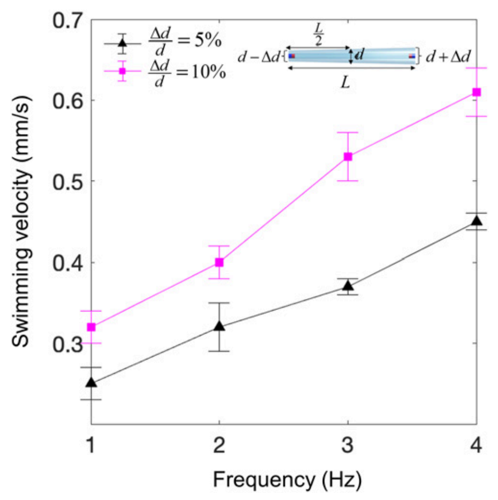

Figure 8. Swimming velocity vs rotating magnetic field frequency for swimming in glycerin solution with varied taper dimension ($\frac{\Delta d}{d}$). At least five trials were performed with each robot for each rotating frequency. Data are presented as mean ± standard deviation.

frequency is applied about the X-axis, an initially straight rod-like soft robot bends and rotates its body (or only the ends) following the rotating field that creates propulsion. Motions both perpendicular (transverse) to and along the magnetic field's rotation axis (X-axis) were observed within both Newtonian fluids. However, propulsion trajectories [figure 5] and velocities [figures 6–8] were affected by the magnitude of the rotating frequency, fluid viscosity, and boundary conditions. When a soft robot is located close to a boundary (i.e., at a distance <5 mm from the workspace boundary or the boundary of the air–fluid interface) and actuates under a uniform rotating magnetic field, the motion is defined as boundary rolling [figure 5(a)] or boundary motion [figure 5(b)]. On the other hand, when a soft robot is located far away from the boundary (i.e., at a distance >15 mm), the motion under a uniform rotating magnetic field is defined as swimming propulsion [figures 5(c)–(e)]. Although the boundary motion (or rolling) is well understood and expected to occur due to the rotation of the soft robot along the boundary, the swimming motion being observed in such highly viscous fluids is interesting. During the swimming propulsion, vertically downward motion (sedimentation due to gravity) along the Z-axis was also observed [figures 5(c) and (e), side views]. In summary, with a rotating magnetic field about the X-axis, a tapered rod-like soft robot located far away from any boundary can swim in viscous fluids, with simultaneous translations along the X-axis, Y-axis (by soft body rotation), and Z-axis (by gravity-driven sedimentation). We will describe all these motions as well as the near boundary propulsions in detail in the following two sections based on experimental observations.

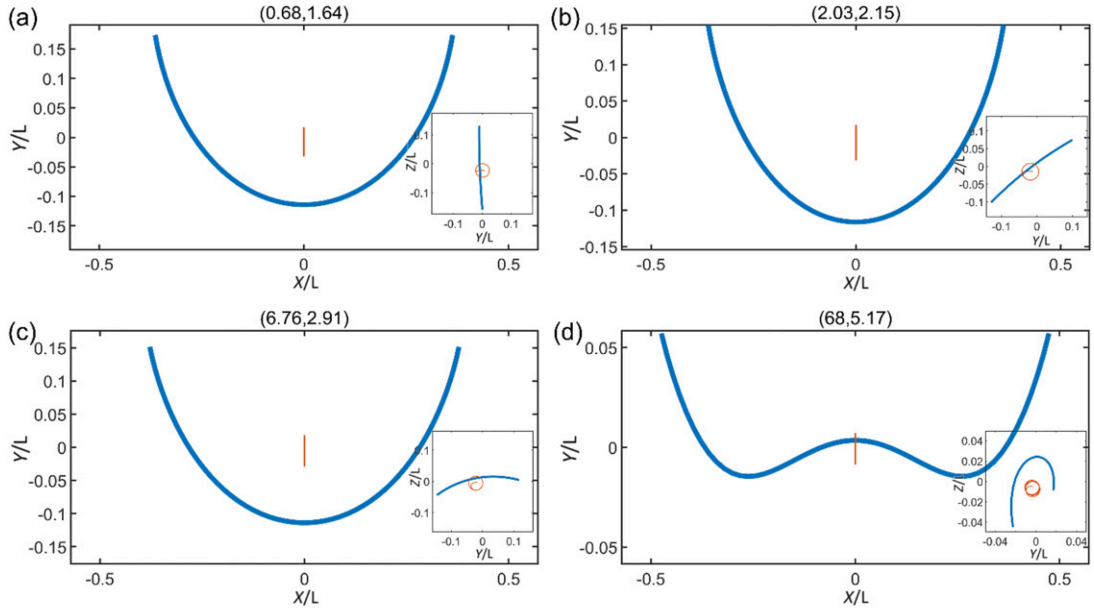

Figure 9. Symmetrically rotating shapes cannot have swimming translation. The steady state deformed shapes of the soft robot are shown in different views for different non dimensional numbers (*Ma*, *Sp*, *Re*) for (a) (0.68, 1.64, 0.06), (b) (2.03, 2.15, 0.02), (c) (6.76, 2.91, 0.006), and (d) (68, 5.17, 0.002). Trajectories of the soft robot (orange lines) indicate that there are no net translations in the X-direction.

3.2. Propulsion near a boundary: boundary rolling

Figures 5(a) and (b) show the motion trajectories of the soft robot (with 5% taper) for near boundary propulsions in glycerin and silicone oil, respectively. When a soft robot is located at the bottom of the workspace (i.e., at a distance <5 mm away from the boundary), and a positive rotation about the X-axis is applied at 1 Hz, the soft robot bends and rolls to create propulsion along the Y-axis [figure 5(a)]. In this case, there is no motion along the Z-axis (sedimentation), as the soft robot is located at the boundary. Figure 6 shows propulsion velocity vs frequency plots for the boundary rolling in glycerin solution. As the rotating magnetic field is applied about the X-axis, both the X- and Y-velocities increase with the increasing rotating frequency up to 4 Hz, then decrease. However, the Y-velocity is observed to be 5× higher than the X-velocity. The rotating frequency of 4 Hz can be interpreted as the step-out frequency [48], beyond which the soft robot cannot rotate in synchrony with the external rotational magnetic field. Above the step-out frequency, the liquid-induced viscous torque ($T \approx -16\pi^2\mu f^3$, where μ and f are the viscosity and rotating frequency, respectively) exceeds the maximum torque that the rotating magnetic field could supply.

Under a rotational magnetic field, a soft robot in glycerin would induce boundary rolling by bending and rolling its entire body [figure 5(a)]; however, a soft robot in silicone oil goes through a complex deformation where only the ends appear to be rotating to create propulsion [figure 5(b)]. The reason may be due to the middle of the soft robot remaining almost straight along the X-axis while only the ends bend, so it appears that only the ends are rotating. A negative rotation of the magnetic field at 1 Hz about the X-axis causes the propulsion of the soft robot along the negative Y-axis [figure 5(b)]. The propulsion velocity of the boundary motion at 1 Hz in silicone oil (0.04 mm s^{-1}) is much smaller than it is for boundary rolling at 1 Hz in glycerin (1.02 mm s^{-1}). Moreover, increasing the rotating frequency from 1 to 2 Hz had no significant effect on the boundary motion in silicone oil, and no propulsion was observed for frequencies over 3 Hz.

3.3. Propulsion far away from any boundary: swimming

A tapered rod-like soft robot ($\frac{\Delta d}{d} = 5\%$ or 10%) in highly viscous fluids (i.e., silicone oil and glycerin) and located far away from any boundary (i.e., at a distance >15 mm from any boundary) is observed to translate in 3D-space under a uniform rotating magnetic field [figures 5(c)–(e)]. However, the rotating frequency and fluid viscosity affect the motion trajectories [figures 5(c)–(e)] and velocities [figures 7 and 8]. We define the propulsion along the X-axis (the rotation axis) as swimming propulsion. During the swimming propulsion, the motions along the Y- and Z-axes are expected to occur due to the interaction of the rotating soft body with the (relatively distant) boundary and gravity-driven sedimentation, respectively. Moreover, the swimming propulsion occurs towards the thick end of the soft robot and is independent of the sense of rotation (i.e., positive or negative rotation).

As shown in figures 5(d) and (e), trajectories at 1 Hz (in glycerin) are observed to be aligned with

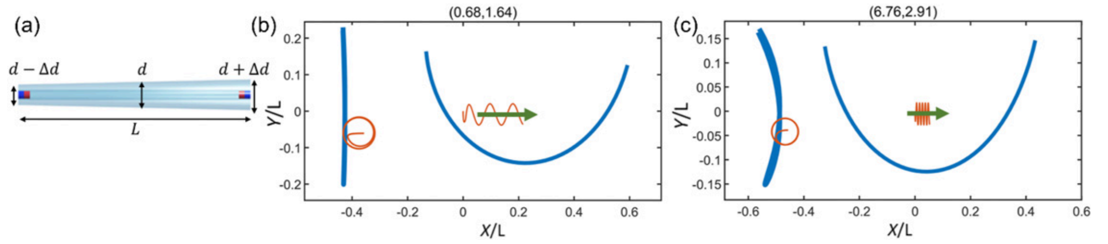

Figure 10. Tapered rods are asymmetric and can have swimming translation. (a) Schematic representation of linear thickness (diameter) variation along the length of a rod-like soft robot. The steady state deformed shapes of the soft robot are shown in different views for different non dimensional numbers (Ma, Sp) for (b) (0.68, 1.64) and (c) (6.76, 2.91). Re values are 0.07 and 0.0002 for (b) and (c), respectively. Trajectories of the soft robot (orange lines) indicate that there are net translations in the X-direction.

the rotation axis. In this case, the soft robot translates only on the X–Z plane [figure 5(e)], and the Y-velocity is insignificant [figure 7(a)]. However, as the rotating frequency increases stepwise from 1 to 10 Hz (with a 1 Hz increment in each step), the trajectories keep shifting towards the Y-axis. The resultant direction of the trajectory comes from the superposition of rolling and swimming motion. Above 4 Hz, the influence of rolling becomes significant [compare X- and Y-velocities in figure 7(a)], so the soft robot goes more diagonally. As a result, the propulsion velocity along the Y-axis increases linearly, almost 7× with the increasing rotating frequency from 1 to 7 Hz [figure 7(a)], then it begins to decrease. On the other hand, the swimming velocity along the X-axis changes much less, increasing only slowly (from 0.25 mm s^{-1} to 0.45 mm s^{-1}) up to 4 Hz before dropping. At the same time, the Z-velocity decreases slightly (from 0.62 mm s^{-1} to 0.55 mm s^{-1}) up to 4 Hz but then proceeds to fluctuate at random. Experiments demonstrated in figure 5(e) and the velocities reported in figure 7 utilized a soft robot with a 5% taper ($\frac{\Delta d}{d} = 5\%$).

To investigate the influence of the taper dimension in the swimming propulsion, we conducted additional swimming experiments (in glycerin) with a soft robot having 10% taper and compared that with the previous results. We found that a rod-like soft robot with 10% taper can achieve higher swimming velocity (along the rotation axis) than a soft robot with 5% taper [figure 8]. As the frequency of the rotation is increased up to 4 Hz, the swimming velocity increases slowly for both robots (from 0.25 mm s^{-1} to 0.45 mm s^{-1} for $\frac{\Delta d}{d} = 5\%$, and from 0.32 mm s^{-1} to 0.61 mm s^{-1} for $\frac{\Delta d}{d} = 10\%$).

As the soft robot is deployed in silicone oil, which has a viscosity of 10 000 cSt ($10\mu_0$), it is observed to be swimming with a positive rotation at 1 Hz about the X-axis [figure 5(c)]; however, the velocities along the X-, Y-, and Z-axes are much smaller compared to what we observed in the glycerin solution [figures 7(b)–(d)]. The velocity decreases because a higher viscosity in silicone oil affects bending in the soft body, ultimately affecting the swimming performance. Moreover, with an increase in the rotating frequency from 1 to 2 Hz, the propulsion velocity in silicone oil only slightly increases along the X-axis [figure 6(b)] while decreasing along the Y- and Z-axes [figures 7(c) and (d), respectively]. In addition, no propulsion is observed for rotating magnetic fields with frequencies over 3 Hz.

Since the gravity-driven sedimentation and rolling (or soft body rotation) are more typical behaviors and do not depend on flexibility to occur, we focus on understanding how the swimming propulsion along the rotation axis is made possible by the flexibility of the soft robot and interesting differences in its dependence on frequency vs viscosity.

3.4. Numerical modeling of the swimming propulsion

To understand how the deformations of rod-like soft robots allow swimming propulsion at low Reynolds numbers, we simulated rods being rotated by an external magnetic field (26 mT) far away from any boundary. The bending stiffness of the rod was chosen to be $EI = 2.11$ mN · mm^2, as indicated by our modeling in section 2.2. Following the experiments, the length of the rod was kept at 10 mm. Magnets with the strength of neodymium 52 (each having a diameter of 0.3 mm and a height of 0.5 mm) were placed at each end, with their south poles oriented towards the ends of the rod.

First, we tested whether a deformation of a symmetric rod with a constant diameter could perform swimming propulsion (i.e., propulsion along the rotation axis). Our simulations using a soft rod of constant diameter 0.8 mm along its length showed that because the two ends of the rod were actuated identically by the magnet, the deformed shape was symmetrical with respect to a plane perpendicular to the rotation axis [figure 9].

However, such a symmetrically rotating shape cannot have an average swimming translation along the rotation axis since both directions along the axis are equivalent. Therefore, a symmetric rod with a constant diameter cannot have swimming propulsion

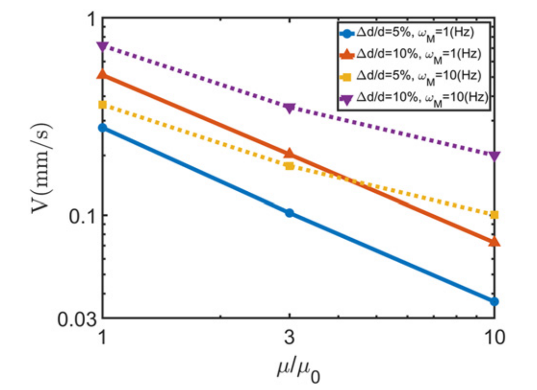

Figure 11. Swimming velocity for different viscosities, rotation frequencies, and taper dimensions.

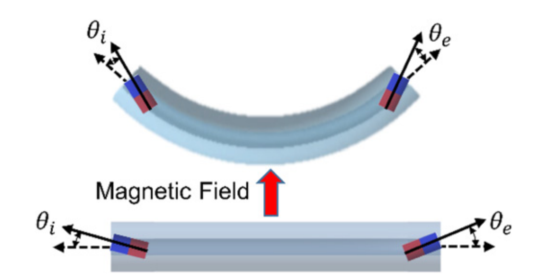

Figure 12. For a constant diameter rod, the magnets at the ends are oriented in different angles to break the symmetry.

even if it is soft and deforms. Achieving swimming propulsion requires breaking this symmetry.

One way we found to break the symmetry was to include a taper in the rod from one end to the other [figure 10(a)]. Our simulations showed that including a taper of 5% or 10% in diameter ($\frac{\Delta d}{d} = 5\%$ or 10%) yielded shapes that deformed so that the shape was no longer symmetric relative to a plane perpendicular to the rotation axis [figure 10]. The observed swimming propulsion was always towards the thicker end of the soft rod, reminiscent of a sperm cell that swims towards the thicker cell body and midpiece of its flagellum. The swimming velocities predicted by our simulations (in a fluid of viscosity $\mu_0 = 1000$ cSt) ranged from 0.2765 mm s^{-1} to 0.5118 mm s^{-1} and from 0.3621 mm s^{-1} to 0.7222 mm s^{-1} for 5% and 10% tapers, respectively [figure 11]. These are on the same order of magnitude as experimentally observed swimming propulsion velocities [figure 8].

A second way we found to break the symmetry of a constant diameter rod was to orient the magnets within the ends of the rod at different angles [figure 12]. We found that in a fluid of viscosity $\mu_0 = 1000$ cSt, even without taper, changing the alignment of one end magnet by 30° led to swimming with a propulsion velocity of 0.650 mm s^{-1}, while changing the alignment of both end magnets by 30° led to swimming with a propulsion velocity of 0.584 mm s^{-1}. Again, both velocities are on the same order of magnitude as experimentally observed swimming propulsion velocities [X-velocity in figure 7(a)].

Our analysis can also explain the observed behavior of swimming propulsion as a function of rotation frequency and viscosity. According to dimensional analysis [49], since the governing equations (4)–(14) only depend on the variables, Ma and Sp, the dimensionless velocity $\frac{U}{\omega L}$ must be some function of those two variables. Thus, a dimensional analysis implies that the swimming propulsion velocity (U) should obey the relation,

$$U = \omega L \tilde{U}(Sp, Ma), \qquad (17)$$

where $\tilde{U}$ is a dimensionless function of the two independent dimensionless parameters. However, since Ma and Sp both depend only on the product of viscosity and frequency ($\mu\omega$), and not viscosity nor frequency separately, changing either viscosity or frequency changes $\tilde{U}$ in the same way. If the frequency is fixed while the viscosity varies, the changes in the dimensional swimming velocity U will reflect the changes in the dimensionless $\tilde{U}$. In our experiments, these reveal a roughly 10× decrease in $\tilde{U}$ as the viscosity increases by 10×. On the other hand, if the viscosity is fixed while the frequency increases by 10×, we expect $\tilde{U}$ to change in the same way, i.e., to decrease by 10×. However, in this case, U is also affected by the prefactor of ω in (17), which cancels the decrease in $\tilde{U}$ to result in a small change in U. Our simulations show the same behavior [figure 11]. For example, for a 5% taper ($\frac{\Delta d}{d} = 5\%$), increasing the viscosity by 10 × (from μ_0 to $10\mu_0$) at a fixed frequency of 1 Hz leads to a 7.5× decrease in velocity at a fixed frequency of 1 Hz (blue data). However, increasing the frequency from 1 Hz to 10 Hz at a fixed viscosity of μ_0 leads to only a 1.3× decrease in the velocity. Similarly, we found that for a soft rod with no taper but with magnets at one or both ends and misaligned by an angle of 30°, increasing the viscosity 10 × (from μ_0 to $10\mu_0$) at a fixed frequency of 1 Hz decreased the velocity by 19× and 22×, respectively; but increasing the frequency from 1 Hz to 10 Hz at fixed viscosity decreased the velocity by only 1.9× and 2.2×, respectively.

4. Conclusion and future work

In this study, we have designed, fabricated, and tested tapered rod-like soft robots which can be actuated by a uniform rotating magnetic field to be propelled by both boundary rolling (perpendicular to the rotation axis) and swimming propulsion (parallel to the rotation axis) in highly viscous Newtonian fluids. Given that rigid rod-like robots would only be capable of boundary rolling propulsion, we used a numerical model to show how the deformation of the rod-like soft robots produces the swimming propulsion.

We showed that the swimming propulsion requires an asymmetry in the rod-like soft robot, such as via a taper in the diameter of the rod (which our soft robots do have) or via a misalignment of the magnets at the end of the rod. Furthermore, dimensional analyses explained why fluid viscosity strongly affects swimming propulsion velocity while changing the rotation frequency has a smaller effect.

Our results suggest possible routes for the improvement of rod-like soft robots. In general, any asymmetry along the rod should lead to swimming propulsion. Therefore, we numerically investigated both an asymmetric soft rod with a taper along its length and with misalignment of the magnets at the ends. Although we cannot observe or control the orientation of the magnets at the ends of the soft robot, we could experimentally validate the effect of the tapered geometry of the rod-like soft robot on the swimming propulsion at low Reynolds numbers. Thus, creating asymmetry in ways other than misaligning the magnets is more practical. For example, embedding magnets at only one end of the rod would create asymmetry that is more extreme than misaligning the magnets at either end. Other promising routes to asymmetry include making one end of the rod thicker or stiffer than the other. Interestingly, biological soft rod-like swimmers naturally have similar geometrical asymmetries, such as sperm cells with a cell body at one end and variable stiffness along their flagella.

Acknowledgments

We would like to thank the National Science Foundation (CMMI #1760642 and #1761060) for funding our research and the University of Utah Center for High Performance Computing for providing the resources to conduct the study. We thank Dr Justyn Jaworski for helping us with the preparation of hydrogel polymer. We thank Dr Louis William Rogowski for his guidance in conducting preliminary experiments.

Author contributions

AB, MJ, HCF, and MJK designed the study; AB fabricated the soft robots and conducted the experiments; AB and GK performed experimental data analysis; MJ and HCF developed the computational model and performed simulation; AB and MJ drafted the manuscript with the help of HCF and MJK; MJK was the principal investigator and provided necessary resources for all experiments.

Data availability statement

All data that support the findings of this study are included within the article (and any supplementary files).

ORCID iDs

Anuruddha Bhattacharjee https://orcid.org/0000-0002-4053-4029
Mehdi Jabbarzadeh https://orcid.org/0000-0003-1809-9793
Gokhan Kararsiz https://orcid.org/0000-0002-0710-1686
Henry C Fu https://orcid.org/0000-0002-3543-7128
Min Jun Kim https://orcid.org/0000-0002-0819-1644

References

[1] Hu W, Lum G Z, Mastrangeli M and Sitti M 2018 Small-scale soft-bodied robot with multimodal locomotion *Nature* **554** 81–5

[2] Lu H, Zhang M, Yang Y, Huang Q, Fukuda T, Wang Z and Shen Y 2018 A bioinspired multilegged soft millirobot that functions in both dry and wet conditions *Nat. Commun.* **9** 1–7

[3] Xu T, Zhang J, Salehizadeh M, Onaizah O and Diller E 2019 Millimeter-scale flexible robots with programmable three-dimensional magnetization and motions *Sci. Rob.* **4** eaav4494

[4] Ren Z, Hu W, Dong X and Sitti M 2019 Multi-functional soft-bodied jellyfish-like swimming *Nat. Commun.* **10** 1–12

[5] Bhattacharjee A, Rogowski L W, Zhang X and Kim M J 2020 Untethered soft millirobot with magnetic actuation *2020 IEEE Int. Conf. Robotics and Automation (ICRA)* (Piscataway, NJ: IEEE) pp 3792–8

[6] Du X, Cui H, Xu T, Huang C, Wang Y, Zhao Q, Xu Y and Wu X 2020 Reconfiguration, camouflage, and color-shifting for bioinspired adaptive hydrogel-based millirobots *Adv. Funct. Mater.* **30** 1909202

[7] Purcell E M 1977 Life at low Reynolds number *Am. J. Phys.* **45** 3–11

[8] Huang H-W, Uslu F E, Katsamba P, Lauga E, Sakar M S and Nelson B J 2019 Adaptive locomotion of artificial microswimmers *Sci. Adv.* **5** eaau1532

[9] Zhang J and Diller E 2018 Untethered miniature soft robots: modeling and design of a millimeter-scale swimming magnetic sheet *Soft Robot.* **5** 761–76

[10] Huang C, Lai Z, Zhang L, Wu X and Xu T 2021 A magnetically controlled soft miniature robotic fish with a flexible skeleton inspired by zebrafish *Bioinspir. Biomim.* **16** 065004

[11] Ali J, Cheang U K, Liu Y, Kim H, Rogowski L, Sheckman S, Patel P, Sun W and Kim M J 2016 Fabrication and magnetic control of alginate-based rolling microrobots *AIP Adv.* **6** 125205

[12] Chen S, Cao Y, Sarparast M, Yuan H, Dong L, Tan X and Cao C 2020 Soft crawling robots: design, actuation, and locomotion *Adv. Mater. Technol.* **5** 1900837

[13] Pancaldi L, Noseda L, Dolev A, Fanelli A, Ghezzi D, Petruska A J and Sakar M S 2022 Locomotion of sensor-integrated soft robotic devices inside sub-millimeter arteries with impaired flow conditions *Adv. Intell. Syst.* **4** 2100247

[14] Pham L N, Steiner J A, Leang K K and Abbott J J 2020 Soft endoluminal robots propelled by rotating magnetic dipole fields *IEEE Trans. Med. Robot. Bionics* **2** 598–607

[15] Gao G, Wang Z, Xu D, Wang L, Xu T, Zhang H, Chen J and Fu J 2018 Snap-buckling motivated controllable jumping of thermo-responsive hydrogel bilayers *ACS Appl. Mater. Interfaces* **10** 41724–31

[16] Li M, Wang X, Dong B and Sitti M 2020 In-air fast response and high speed jumping and rolling of a light-driven hydrogel actuator *Nat. Commun.* **11** 1–10

[17] Wu Y, Dong X, Kim J-k, Wang C and Sitti M 2022 Wireless soft millirobots for climbing three-dimensional surfaces in confined spaces *Sci. Adv.* **8** eabn3431

[18] Bozuyuk U, Yasa O, Yasa I C, Ceylan H, Kizilel S and Sitti M 2018 Light-triggered drug release from 3D-printed magnetic chitosan microswimmers *ACS Nano* **12** 9617–25

[19] Son D, Gilbert H and Sitti M 2020 Magnetically actuated soft capsule endoscope for fine-needle biopsy *Soft Robot.* **7** 10–21

[20] Yim S and Sitti M 2011 Design and rolling locomotion of a magnetically actuated soft capsule endoscope *IEEE Trans. Robot.* **28** 183–94

[21] Runciman M, Darzi A and Mylonas G P 2019 Soft robotics in minimally invasive surgery *Soft Robot.* **6** 423–43

[22] Sitti M 2018 Miniature soft robots—road to the clinic *Nat. Rev. Mater.* **3** 74–5

[23] Dong X, Lum G Z, Hu W, Zhang R, Ren Z, Onck P R and Sitti M 2020 Bioinspired cilia arrays with programmable nonreciprocal motion and metachronal coordination *Sci. Adv.* **6** eabc9323

[24] Ren Z, Zhang R, Soon R H, Liu Z, Hu W, Onck P R and Sitti M 2021 Soft-bodied adaptive multimodal locomotion strategies in fluid-filled confined spaces *Sci. Adv.* **7** eabh2022

[25] Ahmed D, Baasch T, Jang B, Pane S, Dual J and Nelson B J 2016 Artificial swimmers propelled by acoustically activated flagella *Nano Lett.* **16** 4968–74

[26] Kaynak M, Dirix P and Sakar M S 2020 Addressable acoustic actuation of 3d printed soft robotic microsystems *Adv. Sci.* **7** 2001120

[27] Huang C, Lv J-A, Tian X, Wang Y, Yu Y and Liu J 2015 Miniaturized swimming soft robot with complex movement actuated and controlled by remote light signals *Sci. Rep.* **5** 1–8

[28] Shin B, Ha J, Lee M, Park K, Park G H, Choi T H, Cho K-J and Kim H-Y 2018 Hygrobot: a self-locomotive ratcheted actuator powered by environmental humidity *Sci. Rob.* **3** eaar2629

[29] Sitti M, Ceylan H, Hu W, Giltinan J, Turan M, Yim S and Diller E 2015 Biomedical applications of untethered mobile milli/microrobots *Proc. IEEE* **103** 205–24

[30] Nelson B J, Kaliakatsos I K and Abbott J J 2010 Microrobots for minimally invasive medicine *Annu. Rev. Biomed. Eng.* **12** 55–85

[31] Berg H C 2004 *Escherichia Coli in Motion* (Berlin: Springer)

[32] Charon N W and Goldstein S F 2002 Genetics of motility and chemotaxis of a fascinating group of bacteria: the spirochetes *Annu. Rev. Genet.* **36** 47–73

[33] Janda J M, Powers C, Bryant R G and Abbott S L 1988 Current perspectives on the epidemiology and pathogenesis of clinically significant vibrio spp *Clin. Microbiol. Rev.* **1** 245–67

[34] Lauga E and Powers T R 2009 The hydrodynamics of swimming microorganisms *Rep. Prog. Phys.* **72** 096601

[35] Dreyfus R, Baudry J, Roper M L, Fermigier M, Stone H A and Bibette J 2005 Microscopic artificial swimmers *Nature* **437** 862–5

[36] Williams B J, Anand S V, Rajagopalan J and Saif M T A 2014 A self-propelled biohybrid swimmer at low Reynolds number *Nat. Commun.* **5** 1–8

[37] Cheang U K, Meshkati F, Kim D, Kim M J and Fu H C 2014 Minimal geometric requirements for micropropulsion via magnetic rotation *Phys. Rev.* E **90** 033007

[38] Al Khatib E, Bhattacharjee A, Razzaghi P, Rogowski L W, Kim M J and Hurmuzlu Y 2020 Magnetically actuated simple millirobots for complex navigation and modular assembly *IEEE Robot. Autom. Lett.* **5** 2958–65

[39] Cortez R, Fauci L and Medovikov A 2005 The method of regularized Stokeslets in three dimensions: analysis, validation, and application to helical swimming *Phys. Fluids* **17** 031504

[40] Cortez R 2001 The method of regularized Stokeslets *SIAM J. Sci. Comput.* **23** 1204–25

[41] Hyon Y, Marcos T R, Powers T R, Stocker R and Fu H C 2012 The wiggling trajectories of bacteria *J. Fluid Mech.* **705** 58–76

[42] Jabbarzadeh M and Fu H C 2018 Dynamic instability in the hook-flagellum system that triggers bacterial flicks *Phys. Rev.* E **97** 012402

[43] Constantino M A, Jabbarzadeh M, Fu H C and Bansil R 2016 Helical and rod-shaped bacteria swim in helical trajectories with little additional propulsion from helical shape *Sci. Adv.* **2** e1601661

[44] Constantino M A, Jabbarzadeh M, Fu H C, Shen Z, Fox J G, Haesebrouck F, Linden S K and Bansil R 2018 Bipolar lophotrichous helicobacter suis combine extended and wrapped flagella bundles to exhibit multiple modes of motility *Sci. Rep.* **8** 14415

[45] Meshkati F and Fu H C 2014 Modeling rigid magnetically rotated microswimmers: rotation axes, bistability, and controllability *Phys. Rev.* E **90** 063006

[46] Martindale J D, Jabbarzadeh M and Fu H C 2016 Choice of computational method for swimming and pumping with nonslender helical filaments at low Reynolds number *Phys. Fluids* **28** 021901

[47] Jabbarzadeh M and Fu H C 2020 A numerical method for inextensible elastic filaments in viscous fluids *J. Comput. Phys.* **418** 109643

[48] Mahoney A W, Nelson N D, Peyer K E, Nelson B J and Abbott J J 2014 Behavior of rotating magnetic microrobots above the step-out frequency with application to control of multi-microrobot systems *Appl. Phys. Lett.* **104** 144101

[49] Gerhart P M, Gerhart A L and Hochstein J I 2016 *Munson, Young and Okiishi's Fundamentals of Fluid Mechanics* (New York: Wiley)